Mass Transport across the Porous Oxide Shells of Core-Shell and Yolk-Shell Nanostructures in Liquid Phase

6 AUTHORS, INCLUDING:

Xiaoliang Liang
Chinese Academy of Sciences
24 PUBLICATIONS **380** CITATIONS

SEE PROFILE

Ji-Bong Joo
Korea Institute of Energy Research
72 PUBLICATIONS **1,727** CITATIONS

SEE PROFILE

Yadong Yin
University of California, Riverside
269 PUBLICATIONS **23,260** CITATIONS

SEE PROFILE

Francisco Zaera
University of California, Riverside
**376** PUBLICATIONS **12,192** CITATIONS

SEE PROFILE

Mass Transport across the Porous Oxide Shells of Core−Shell and Yolk−Shell Nanostructures in Liquid Phase

Jie Li,[†] Xiaoliang Liang,[‡] Ji Bong Joo, Ilkeun Lee, Yadong Yin, and Francisco Zaera*

Department of Chemistry, University of California, Riverside, California 92521, United States

ABSTRACT: The mass transport of a number of molecules dissolved in a liquid solvent through the shells of $Pt@SiO_2$ core−shell and $Pt@Void@TiO_2$ yolk−shell nanostructures was characterized in situ by infrared absorption spectroscopy. Our samples, which were used here to represent the core−shell and yolk−shell nanostructures that have become so popular in recent times, were determined to exhibit a dual distribution of pore sizes, with a majority of micropores with diameters of less than 1 nm and a second group of mesopores with windows approximately 4 nm in diameter. The uptake of carbon monoxide from CCl_4 or ethanol solutions onto the surface of the metal of these nanostructures was characterized first. It was determined that adsorption is possible with both samples, and that saturation on the metal surface precedes saturation on the oxide shell. This latter observation suggests that the access of the CO molecules (and all other molecules studied here) to the inside of the yolk−shell structures may be controlled by the mass transport of the liquid through the porous network of the shells, not by the diffusion of the dissolved gas alone. Additional studies were carried out with a family of cinchona alkaloid derivatives and with a porphyrin, covering a range of molecular sizes of approximately 5−20 Å in diameter. Adsorption of all those molecules on the Pt surfaces of both nanoarchitectures was deemed possible by a combination of tests, including the detection of changes in peak frequencies or peak intensities and measurements of the reversibility of the adsorption. Our results indicate that although the sol−gel synthetic method used to prepare the shells usually produces solids with microporous structures, a secondary mesoporous network that also develops in these nanostructures can provide a direct path to the metal nanocores, affording the mass transport of large molecules in liquid solutions in and out of the inside volumes. We also show that the attoliter-size volumes encased by typical shells in yolk−shell nanostructures are sufficient to afford adsorption displacement processes.
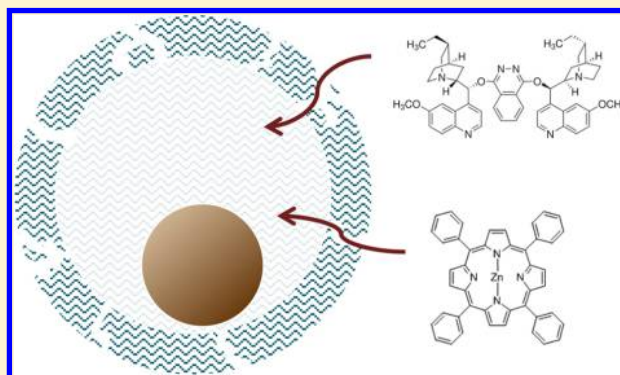
1. INTRODUCTION

Much work has been dedicated recently to the synthesis of designed complex nanostructures.[1] Many of these projects have relied on the growth, often via sol−gel chemistry, of porous oxides on specific underlying structures.[2] Core−shell and yolk−shell nanoarchitectures, in which a core nanoparticle is encapsulated by an outer layer of a second material, have been particularly popular because they offer great promise in a multitude of applications, including sensing,[3−5] drug delivery and biomedical imaging,[6−8] catalysis and electrocatalysis (including fuel cells),[9−11] and the development of batteries[12] and energy storage devices.[13]

The shell in core−shell and yolk−shell nanostructures can protect the core element from the outside environment, help maintain its compositional and structural integrity and prevent its aggregation or sintering into large particles, allow for the selective percolation of molecules in and out of the interior of the shell, and increase the solubility and/or biocompatibility or change or add other physical or chemical properties to the overall structure.[14−16] In yolk−shell nanostructures, the void inner space between the core and the shell can also serve as a reservoir for specific substances or as an individualized attoliter-sized reactor.[17−19]

Many applications of these nanostructures are engineered around the idea of the controlled transport of specific molecules across the shells, which in such context may act as a semipermeable membrane. Hollow shells may be used to slowly deliver drugs or other key molecules to a specific outside environment, for example, or the reactants may be required to diffuse into the interior volume of yolk−shell catalysts to access the core nanoparticle, which may act as the catalytic phase. The potential limited diffusivity of the molecules of interest through the shells, which may be particularly restricted in liquid phase, may affect the performance of the overall nanostructure. Surprisingly, though, very little work has been carried out to directly test the transport properties of these shells to date. In many instances such evaluation has been performed indirectly, by testing the performance of the nanostructures for the application at hand, but in those cases the final answer may be masked by other interfering factors.

Here we report on an approach that relies on the use of probe molecules and their ability to adsorb on the surface of the

core nanoparticles: it is inferred that adsorption on the surface of the metal core reflects transport of such probe molecules through the oxide shells of core−shell and yolk−shell nanostructures. The adsorption is evaluated in situ, in liquid phase, by infrared absorption spectroscopy. A couple of early reports have relied on the use of carbon monoxide to test the uptake on metal nanocores in the gas phase.[20,21] Probing adsorption in situ at the liquid−solid interfaces is much more difficult[22−24] but has also been recently accomplished by our group: initial results from work on the detection of CO adsorbed from a liquid phase onto the core of core−shell and yolk−shell nanostructures have shown that such studies are now possible.[25] In all the cases reported so far, which have all involved carbon monoxide uptake, adsorption on the core metal takes place readily, presumably because CO is a small molecule that can easily diffuse through the porous structure of the surrounding oxide shells. In this report we expand on our initial report in order to test the transport of a number of more complex dissolved molecules of various sizes and shapes.

The present work goes beyond a simple extension of the previous work by focusing on the characterization of samples in situ in liquid phase by adsorbing not only CO but also larger organic molecules. For this, two main qualitative changes needed to be addressed: (1) the spectroscopic (IR) signals for organic molecules are orders of magnitude weaker than those from CO, a fact that makes their detection much harder, and (2) the organic compounds used as probes here are either solids or liquids, not a dissolved gas as is the case with CO. It also became clear that it is important in these experiments to develop ways to differentiate between adsorbed and dissolved species and between adsorption on the surfaces of the metal core versus the oxide shell. Consequently, different approaches had to be devised to evaluate adsorption for each individual molecule. For instance, the different time evolution of the signals from adsorption on the metal versus the oxide surfaces was used to establish that the transfer of molecules inside the shells occurs via mass transport of the whole solution, not by diffusion of the solute within the solvent. We also report on the ability of molecules dissolved in solution to displace other adsorbates within the confined volume of the shells in yolk−shell nanostructures. In more general terms, it was found that, by and large, diffusion through the shells of core−shell and yolk−shell nanostructures is relatively easy for molecules with dimensions of up to approximately 2 nm. A more detailed discussion of these is provided below.

2. EXPERIMENTAL SECTION

Two types of solid samples were tested in this study: a Pt@SiO$_2$ core−shell nanostructure and a Pt@Void@TiO$_2$ yolk−shell nanoarchitecture. The starting point in both cases was a solution of 5-nm Pt nanoparticles, which were prepared by adding an aqueous solution of H$_2$PtCl$_6$·6H$_2$O (0.386 M, 0.137 mL, Alfa, 99.9% purity) to deionized water (30 mL) and heating that to its boiling point. A sodium citrate solution (3 wt %, 2 mL, Sigma-Aldrich, ≥99% purity) was added, and the resulting mixture was stirred for 1 h. Upon cooling down to room temperature, polyvinylpyrrolidone (PVP, 0.3 g, MW = 40 000, Sigma-Aldrich) was added, and the solution was kept overnight under stirring to allow for the adsorption of PVP on the Pt surface.

The Pt@SiO$_2$ samples were prepared by growing a SiO$_2$ layer around those citrate-stabilized 5-nm-diameter Pt nanoparticles via a sol−gel process using tetraethyl orthosilicate (TEOS,

Aldrich-Sigma, 98% purity). 4 mL of the above-mentioned PVP-treated Pt solution was sequentially mixed with ethanol (23 mL), TEOS (4.3 mL) and an aqueous solution of ammonia (28%, 0.62 mL), and the reaction mixture was stirred for 4 h at room temperature. Silica shells approximately 50 nm in diameter were grown for the studies reported here. The resulting Pt@SiO$_2$ particles were separated by centrifugation and washed three times with ethanol, and the particles were redispersed in ethanol (20 mL) under sonication. Finally, porosity was achieved by adding a PVP surfactant to protect the outer layer while etching with NaOH in a controlled fashion.[19]

To make the Pt@Void@TiO$_2$ nanostructures, similar Pt@SiO$_2$ samples were prepared, in this case of approximately 200 nm in diameter, but instead of etching the silica shell right away, an outer titania shell was grown on top first by using a similar sol−gel process but with titanium(IV) butoxide (TBOT, Sigma-Aldrich, 97% purity). The Pt@SiO$_2$ solution (5 mL) was dispersed in a mixture containing hydroxypropyl cellulose (HPC, 100 mg), ethanol (20 mL), and water (0.12 mL). After the reaction mixture had been stirred for 30 min, a solution of TBOT (1 mL) dissolved in ethanol (4.5 mL) was slowly added using a syringe pump (0.5 mL/min), and the temperature was then increased to 358 K while the reaction mixture was stirred for 90 min under reflux conditions. The precipitate containing the Pt@SiO$_2$@TiO$_2$ nanocomposites was collected using centrifugation, washed with ethanol, and redispersed in deionized water (20 mL).

The Pt@SiO$_2$@TiO$_2$ samples were coated with a second protective silica layer to help with the stability of the titania shells during calcination. PVP (MW = 40 000, 0.2 g) was added into the solution, which was then kept overnight under stirring to allow for the adsorption of PVP on the TiO$_2$ surface. The PVP-treated Pt@SiO$_2$@TiO$_2$ particles were separated using centrifugation, washed, redispersed in ethanol (5 mL), and mixed with more ethanol (18 mL), TEOS (0.86 mL), and an aqueous solution of ammonia (28%, 0.62 mL), and the reaction mixture was stirred for 4 h. The resulting Pt@SiO$_2$@TiO$_2$@SiO$_2$ particles were separated by centrifugation, washed three times with ethanol and dried under vacuum, and calcined in air at 173 K for 2 h to crystallize the amorphous TiO$_2$ to anatase TiO$_2$.

The sacrificial silica layer was then etched away using an aqueous solution of NaOH.[19,21,26] After heating to 363 K, a NaOH solution (2.5 M, 4 mL) was added to the above solution, and the mixture was stirred for 2 h to completely remove the silica. The resulting Pt@Void@TiO$_2$ yolk−shell particles, which in the cases reported here were made with 20 nm thick shells, were separated by centrifugation, washed five times with deionized water and twice with ethanol, and dried. Finally, the platinum nanoparticles were grown to a size of approximately 30 nm in diameter. A Pt@Void@TiO$_2$ sample (50 mg) was well mixed with deionized water (10 mL) and hydrazine (0.05 mL) under stirring. An aqueous solution of H$_2$PtCl$_6$·6H$_2$O (0.1 M, 0.13 mL) mixed with a NaNO$_2$ solution (1 M 0.6 mL) in deionized water (4 mL) was slowly added using a syringe pump (0.25 mL/min). After stirring for 30 min, the precipitate was collected using centrifugation, washed with water and ethanol, and dried.

Typical transmission electron microscopy (TEM) images of both samples are shown in Figure 1. A number of reference catalysts were prepared as well, including a 1 wt % Pt/SiO$_2$ conventional catalyst and a Void@TiO$_2$ empty shell nanostructure. The first was made by impregnation of a commercial SiO$_2$
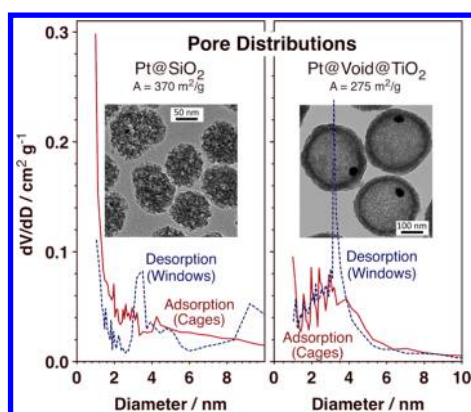
B

dx.doi.org/10.1021/jp406991y | J. Phys. Chem. C XXXX, XXX, XXX−XXX

Figure 1. Pore distributions in our Pt@SiO$_2$ (left) and Pt@Void@TiO$_2$ (right) core–shell and yolk–shell nanostructures, as determined by N$_2$ BET adsorption isotherm measurements. Distributions measured from both the adsorption (solid red lines) and desorption (dashed blue) branches, reflecting the diameters of the inside pores and the connecting windows, respectively, are reported. Total surface areas and typical transmission electron microscopy (TEM) images are also provided. It was determined that the porosity of these samples is dominated by micropores of less than 1 nm in diameter, but that there is also a secondary mesoporous network with diameters around approximately 4 nm.

powder (Aerosil 200, 99.8%, surface area = 100 ± 25 m^2/g) with an aqueous solution of H$_2$PtCl$_6$·6H$_2$O. The slurry made out of the solution and the silica were stirred at room temperature for a few hours and then slowly dried at 353 K. The resulting pale yellow fine powder was calcined at 673 K for 4 h in air to obtain a gray powder. The Void@TiO$_2$ nanostructures were prepared in a similar way as the Pt@Void@TiO$_2$ samples except that the first step, the addition of the Pt nanoparticles, was skipped.[27]

Adsorption on the Pt nanoparticles was followed by using an in-situ infrared (IR) absorption spectroscopy cell initially designed for reflection–absorption infrared spectroscopy (RAIRS) studies at the solid–liquid interface,[28] The IR beam from a Fourier-transform infrared (FTIR) spectrometer is sent through a linear polarizer and focused through a transparent trapezoidal CaF$_2$ prism onto a polished back disk (∼1 cm in diameter), which is mounted on a movable supporting rod and pressed against the far surface of the prism; the liquid solution is trapped as a thin film in between those two surfaces. The reflected light is then collected and refocused onto a mercury cadmium telluride (MCT) detector. Spectra are acquired with both p- and s-polarized light to discriminate against the species adsorbed on the back surface, which, according to a well-established surface-selection rule,[29,30] only absorb p-polarized light.

The original RAIRS arrangement was modified here to operate in transmission mode by using a polished copper surface as the back mirror and by trapping suspensions of the nanostructures to be studied in solution in between that mirror and the front optical prism.[28,31] Briefly, a small amount of the catalyst (typically 3 mg) was placed on the copper piece and pressed against the prism, at a fixed distance of 0.1 mm. The cell was assembled and placed in the FTIR setup, and the optics was aligned for maximum signal. The pure solvent, typically CCl$_4$, was added, and reference IR spectra were acquired with both p- and s-polarized light. Hydrogen was bubbled next for 60 min to activate the catalyst, and the solvent was flushed with the solution of interest. New p- and s-polarized spectra were

acquired at 15 min intervals. The s-polarized data are reported here: that polarization was used to eliminate any possible interference from adsorption on the copper mirror. All the reported spectra correspond to averages from 256 scans, taken with 4 cm^{-1} resolution.

The compounds used as probes for adsorption, 6-methoxyquinoline (6MeOQ, 98% purity), cinchonidine (Cd, 96% purity), hydroquinidine-4-chlorobenzoate (H4C, 98% purity), hydroquinidine-4-methyl-2-quinolyl ether (H4M2QE, 97% purity), hydroquinine 1,4-phthalazinediyl diether ((DHQ)2PHAL, >95% purity), and meso-tetraphenylporphyr-in zinc (ZnTPP), were all purchased from Sigma-Aldrich and used as provided. CCl$_4$ was chosen as the solvent in most experiments because of the limited number of absorption bands that it exhibits in the IR spectra, which minimizes interference with the much smaller signals of the solutes and adsorbates. Large peaks were nevertheless detected at 1229, 1251, and 1551 cm^{-1}, which partially blocked the information collected in the 1100–1800 cm^{-1} frequency window. CO adsorption was also tested in ethanol.

3. RESULTS AND DISCUSSION

3.1. Sample Characterization. The physical characteristics of the core–shell and yolk–shell samples prepared in this study were evaluated first. Specifically, their surface area and pore distribution were assessed by BET measurements. Figure 1 displays the main results. Pore distributions were calculated from both adsorption and desorption branches of the adsorption isotherms to obtain information about the size of the inside of the pores and the interconnecting windows, respectively. Both samples display significant surface areas, on the order of several hundred square meters per gram, a range typical of silica and other oxides used in catalysis. As expected from their sol–gel synthesis, they show significant micro-porosity, with diameters below 1 nm. This is particularly true for the Pt@SiO$_2$ catalysts, where microporosity is in fact dominant. It would be reasonable to expect that the predominance of micropores of less than 1 nm in diameter may limit the adsorption of large molecules onto the surface of the metal core. However, both nanostructures also show mesoporosity, especially in terms of the connecting windows, with maxima at approximately 4 nm in diameter. The mesoporous networks are likely the results of defects created by the partial crystallization of the oxide shells during calcination, as indicated by TEM data obtained in the past for similar systems.[32] Mesopores can potentially offer a way for large molecules to diffuse into the inside of the core–shell and yolk–shell nanoarchitectures. It is this adsorption that was tested here—the main subject of our report.

3.2. Carbon Monoxide Adsorption. Typical infrared absorption spectra obtained for the uptake of carbon monoxide from CCl$_4$ solutions onto platinum surfaces are shown in Figure 2. The reported data correspond to the C–O stretching region of linearly adsorbed CO, between approximately 2000 and 2200 cm^{-1}, and are displayed for three samples, namely, a regular 1 wt % Pt/SiO$_2$ (left panel) catalyst and our Pt@SiO$_2$ (center) and Pt@Void@TiO$_2$ (right) nanostructures, as a function of the time of exposure to the CO-saturated solutions. It is clear that in all cases significant adsorption is seeing over time, as manifested by the appearance of sharp peaks in the appropriate C–O stretching region. With Pt/SiO$_2$, the peak starts at about 2080 cm^{-1} and blue-shifts slowly as the surface coverage increases with increasing exposure time, until reaching
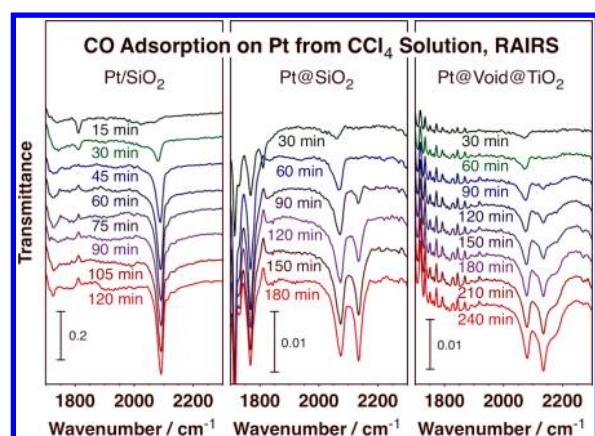
Figure 2. Transmission infrared (IR) absorption spectra for carbon monoxide adsorption on three types of platinum-based samples, namely, a conventional 1 wt % Pt/SiO$_2$ catalyst (left panel), and Pt@SiO$_2$ core–shell (center) and Pt@Void@TiO$_2$ yolk–shell (right) nanostructures. Shown are series of spectra in the C–O stretching region as a function of time of exposure to a CO-saturated CCl$_4$ solution. In addition to the on-top adsorption state on platinum seen at approximately 2060–2090 cm^{-1} in all three cases, additional features are also observed at 2135 cm^{-1} with both nanostructures, and a third 2180 cm^{-1} peak is detected in the Pt@Void@TiO$_2$ case as well. The latter features are due to adsorption on the support, which were shown to be weak and reversible.

a value of 2092 cm^{-1}. A second weak and broad feature also appears around 1920 cm^{-1}, associated with CO bridge-bonded to platinum. All these observations are consistent with adsorption on Pt/SiO$_2$ catalysts from the gas phase[33−35] and also with CO adsorption on other types of Pt catalysts immersed in solution.[31]

Equivalent peaks are seen with the nanostructured samples. With Pt@SiO$_2$, the C–O stretching peak of the carbon monoxide adsorbed in on-top sites on the platinum surface is already clearly seen after the first 30 min of exposure to the CO/CCl$_4$ solution, as a broad asymmetric feature with a maximum at 2060 cm^{-1}, and shifts to 2077 cm^{-1} after 180 min. In the Pt@Void@TiO$_2$ case, the early signal is centered at 2070 cm^{-1} and shifts to a final value of 2080 cm^{-1}. These trends parallel that seen with Pt/SiO$_2$, except for small differences in the absolute values of the stretching frequencies, which may be explained by differences in the electronic nature of the support surrounding the platinum nanoparticles. In addition, however, a second set of peaks is seen with both core–shell and yolk–shell samples, associated with adsorption on the support. For Pt@SiO$_2$, this shows up as a single peak at 2135 cm^{-1} that first appears after 90 min of CO/CCl$_4$ exposure and that grows but does not shift after longer exposure times. With Pt@Void@TiO$_2$, a similar 2135 cm^{-1} peak is accompanied by a high-frequency shoulder at about 2180 cm^{-1}. These features are not seen with Pt/SiO$_2$ and are likely associated with Na$^+$ ions in the oxide resulting from ion exchange during the NaOH etching step in the synthesis of the nanostructures. The CO identified by these IR latter peaks is adsorbed only weakly and reversibly on the surface, and is easily removed by flushing with pure CCl$_4$ (the CO bonded to the platinum remains adsorbed after such treatment).

The detection of CO adsorption on our nanostructures, as seen in Figure 2, indicates easy accessibility to the surface of the metal by CO molecules coming from the outside of the shell. In order to evaluate the kinetics of the required mass transport

through the shell, time-resolved data such as those in Figure 2 were analyzed in more detail. The time evolution of the intensity of the CO features in the IR spectra is reported for a set of representative samples in Figure 3. Collectively, the data
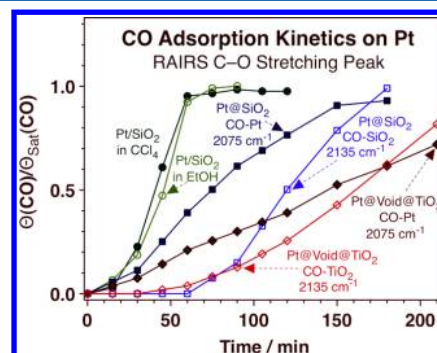

Figure 3. Kinetics of CO adsorption on representative samples, determined from the peak intensities in IR spectra such as those reported in Figure 2. Shown are the uptake curves for CO adsorption on the Pt surfaces in Pt/SiO$_2$ (green circles), Pt@SiO$_2$ (solid dark blue squares), and Pt@Void@TiO$_2$ (solid dark red diamonds) catalysts. The studies with Pt/SiO$_2$ were carried out with two different solvents, CCl$_4$ (solid dark green circles) and ethanol (open light green circles): the similar time behavior obtained in both cases indicates that the nature of the solvent is not critical in these kinetic measurements. Additional data are reported for the adsorption of CO on the silica (open light blue squares) and titania (open light red diamonds) shells of the corresponding two nanostructures. CO saturation takes longer on the Pt inside the shells than in the exposed Pt in Pt/SiO$_2$, but even longer on the shells, suggesting that mass transport of the liquid through the porous structures is what slows down the uptake.

show that there is an induction period of about 15−30 min before significant adsorption takes place. This is an intrinsic limitation of our experimental setup that originates from the way the measurements are carried out, since the solid sample is exposed to only the thin (~100 μm) film of the liquid trapped between the prism and the mirror, and flow through that space is controlled by the limited conductance. After the initial 30 min, though, the results obtained with the regular Pt/SiO$_2$ catalyst indicate that saturation can be achieved relatively quickly, within a period of another 30 min or so. Similar results were obtained in CCl$_4$ (filled dark green circles) and in ethanol (open light green circles), indicating that the measurements are not limited by the nature of the solvent.

The kinetics obtained with the nanostructured catalysts was measurably slower: CO saturation of the Pt surface takes at least 150 min in the case of the Pt@SiO$_2$ sample (solid dark blue squares) and even longer, more than 220 min, with Pt@Void@TiO$_2$ (solid dark red diamonds). This highlights the fact that additional mass transport factors play a role in those systems. It could be though that the slow CO uptake is due to limited diffusion of the CO through the shells, but it is more likely to come from the slow mass transport of the whole CO/CCl$_4$ solution. First, similar uptake times were measured with the other adsorbates reported in this study (as discussed below). Second, the CO uptake with Pt@SiO$_2$ is faster than with Pt@Void@TiO$_2$, in spite of the fact that the shells in the former case are thicker and contain smaller pores than in the latter. We argue that the slow evolution seen with Pt@Void@TiO$_2$ may be due to a dilution effect that takes place in the void space inside the titania shells, which is initially filled with pure CCl$_4$. Finally, with both nanostructures, the saturation of the IR
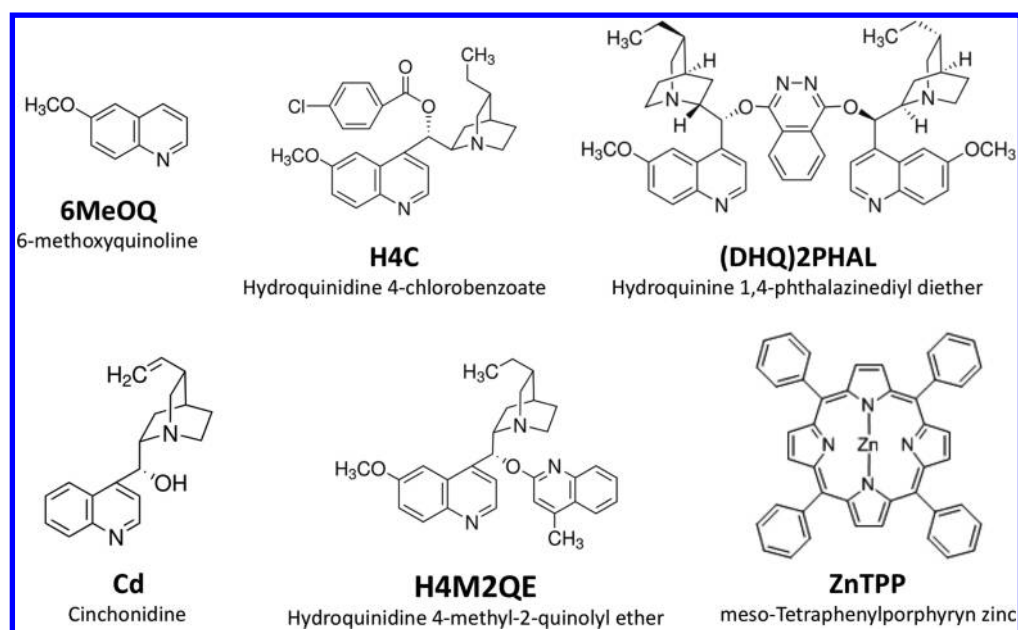
Figure 4. Molecular structures of the compounds used in the adsorption experiments in this report.

signals due to CO adsorbed on the support (open light blue squares and open light red diamonds, respectively) takes even longer times than on the Pt surfaces. Notice in particular that the signals for adsorption on the oxides do not reach saturation even after the 210 min reported in these experiments; their coverage may therefore be overestimated in this figure (we do not have true values for $\Theta_{Sat}(CO)$ for those cases). Since adsorption on the supports is weak, the measured CO coverages may be the result of a dynamic balance of adsorption and desorption rates between the adsorbates and the CO in solution, which may be affected by a slow mixing of the newly added CO-saturated/CCl_4 solution with CO-depleted/CCl_4 solutions surrounding the Pt nanoparticles due to local CO removal upon adsorption or to dilution with the original pure CCl_4 in the cell.

3.3. Adsorption of Other Molecules. Carbon monoxide is a common adsorption probe, in great part because it is easy to handle and detect. However, CO is also a small molecule that can easily diffuse through micropores, even through the less-than-1-nm-in-diameter pores present in most core–shell and yolk–shell nanostructures. As a consequence, CO is not a particularly discriminating choice of probe molecule for mass transport studies. Moreover, in many of the potential applications of our type of core–shell and yolk–shell nanostructures, especially in cases where the operation is to be carried out in the liquid phase (like in pharmaceutical or sensing applications, for instance), larger molecules are likely to be involved. In order to test the mass transport through the shells of our nanostructures under more realistic conditions, the uptake of a number of aromatic and cinchona–alkaloid based molecules was studied in situ in liquid solutions. The general cinchona motive used here stems from our particular interest in using those structures as chiral modifiers for enantioselective catalysis,[36−38] but the results from this work are expected to be more general and to provide a semiquantitative picture of the mass transport limitations associated with core–shell and yolk–shell nanostructures as a function of the size and shape of the molecules involved. The structures of the specific molecules used here are provided in Figure 4, and some of their relevant

physical properties are given in Table 1. Molecular diameters in this set have been estimated to go from approximately 0.7 to 1.9 nm.

Table 1. Molecular Parameters of the Molecular Probes Used in the Studies Reported Here

compound	ρ (g cm^{-3})	MW (g mol^{-1})	V_{molec} (Å^3)	d^a (Å)
6MeOQ	1.1665	159.18	226.5	7.6
Cd	1.2	294.43	407.2	9.2
H4C	1.535	464.98	502.8	9.9
H4M2QE	1.23	467.60	631.0	10.7
(DHQ)2PHAL	1.301	778.98	993.8	12.4
(H2)TPP	1.27	614.74	803.4	11.5 (18.5)^b

^{a}Assuming spherical geometry. ^{b}Assuming cylindrical geometry with 3 Å thickness.

3.3.1. 6-Methoxyquinoline. Figure 5 reports some key results from the studies carried out with 6-methoxyquinoline (6MeOQ). Shown are spectra obtained after saturation of a Pt@Void@TiO$_2$ sample with 6MeOQ using a 0.5 mM solution in CCl_4 (bottom, solid blue trace) and following several flushes with pure CCl_4 to remove any weakly adsorbed species (second from bottom, solid red). Reference spectra are also provided for a 0.1 M 6MeOQ solution in CCl_4 (second from top, dashed blue line) and for 6MeOQ adsorbed on a flat platinum polycrystalline foil from a 10 mM CCl_4 solution (top, dashed red).[39] Several aspects of the chemistry of these systems become apparent from analysis of these data. First, several easy-to-detect peaks are seen in the spectrum obtained for the catalyst immersed in the 6MeOQ solution. However, some of those may originate from molecules in the liquid phase; it is certainly not straightforward to separate the signals from dissolved versus adsorbed molecules. This is why the IR trace obtained after flushing with the clean solvent is also provided; the remaining features following such a treatment must belong to adsorbed species. That still leaves questions about weakly versus strongly adsorbed species, but those may be expected to
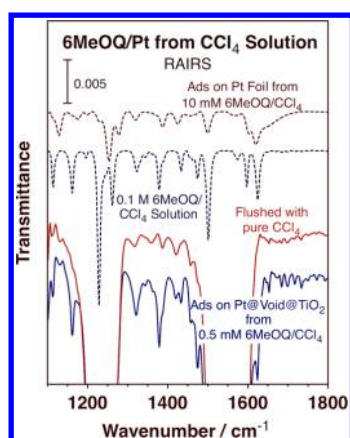
Figure 5. Transmission infrared (IR) absorption spectra for 6MeOQ adsorbed from a CCl_4 solution onto the platinum surface in a Pt@Void@TiO_2 sample. The two bottom spectra correspond to a 3 mg of the catalyst immersed in a 0.5 mM 6MeOQ solution for 180 min (bottom, solid blue) and after flushing the same sample 6 times with pure CCl_4 (second from bottom, solid red). Reference spectra are also shown, for a 0.1 M 6MeOQ solution in CCl_4 (second from top, dashed blue), and for 6MeOQ adsorbed from a 10 mM 6MeOQ CCl_4 solution onto a flat polycrystalline Pt surface (top, dashed magenta).[39] Strong adsorption on the platinum surface is clearly indicated by the very different spectra obtained compared to those for the solution and in the case of the Pt@Void@TiO_2 by the permanence of the signals associated with adsorbed 6MeOQ after flushing with the pure solvent.

Figure 6. Transmission IR absorption spectra from studies on the interdisplacement between 6MeOQ and Cd on the Pt surface of Pt@Void@TiO_2 yolk−shell nanostructures. The bottom six solid traces correspond to the sequential exposure of the sample to (from bottom to top): a 0.5 mM 6MeOQ solution (180 min, green), pure CCl_4 (6 flushes, blue), a 1 mM Cd solution (210 min, purple), pure CCl_4 (5 flushes, red), a 0.5 mM 6MeOQ solution again (210 min green), and pure CCl_4 (5 flushes, blue). The top four reference spectra, shown as dashed traces, correspond to (from top to bottom): a solid Cd sample (red), a Pt polycrystalline foil exposed to a 2 mM Cd/CCl_4 solution (purple),[40] a 0.1 M 6MeOQ solution (green), and a Pt polycrystalline foil exposed to a 10 mM 6MeOQ/CCl_4 solution (blue).[39] The data indicate that Cd from solution can displace 6MeOQ from the Pt surface in Pt@Void@TiO_2, as on Pt foils, but that further exposure to a 6MeOQ solution results in a Cd + 6MeOQ coadsorbed mixture in the former sample, as opposed to the case of the Pt foil, where no additional 6MeOQ uptake is possible.[41]

exhibit some differences in peak position or relative intensities as compared with the data from the 6MeOQ solution. Based on this assessment, the peaks seen at 1115, 1163, 1322, 1379, 1435, 1475, and 1624 cm^{-1} in the spectrum taken in the presence of the 6MeOQ solution are traced back directly to dissolved 6MeOQ. On the other hand, the spectrum from the flushed sample displays features at 1128, 1320, 1384, and 1423 cm^{-1} that match nicely those seen on the flat Pt foil. There is no doubt that 6MeOQ adsorbs molecularly on the surface of the Pt nanoparticles inside the Pt@Void@TiO_2 nanostructures and that that adsorption is irreversible at room temperature. There is no evidence for 6MeOQ adsorption on the titania shell.

3.3.2. Displacement Experiments with Cinchonidine. One potential advantage of yolk−shell nanostructures is that they have a built-in volume that can act as a attoliter-sized reactor containing individual core nanoparticles. However, it is not clear if such volumes are sufficiently large to not interfere with the chemistry of interest. That question was tested here by looking into the possibility of driving simple adsorbate displacement processes. In Figure 6, data are reported for the case of the interdisplacement between 6MeOQ and Cd. Our Pt@Void@TiO_2 yolk−shell sample was sequentially exposed to CCl_4 solutions of 6MeOQ, Cd, and back to 6MeOQ, with added flushes in between using pure CCl_4 to minimize crosstalk between the two types of solutions. The resulting IR data are given by the bottom six traces in Figure 6 (solid lines). Reference spectra are also provided for 6MeOQ and Cd in solution and adsorbed on polycrystalline Pt[39,40] (top four dashed-line traces) to help differentiate between the dissolved species and those adsorbed on the surface.

The first two traces, corresponding to the cases where the yolk−shell nanostructure is exposed to the 6MeOQ solution (bottom, green solid line) and after a pure CCl_4 flush (second from bottom, blue), are equivalent to those in Figure 5
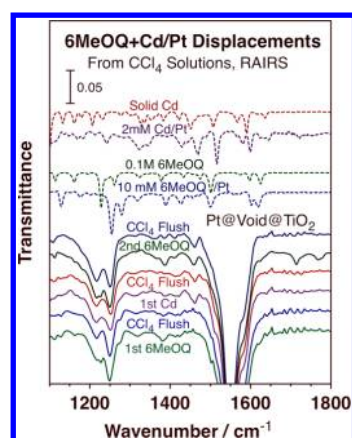
(although acquired in a separate experiment). The second trace in particular indicates the adsorption of 6MeOQ on the platinum nanocores (the peaks are small in Figure 6 because of the change of scale compared to that used in Figure 5). Subsequent exposure of that surface to a Cd solution (third trace from bottom, purple) leads to the displacement of the adsorbed 6MeOQ by newly adsorbed Cd, which also adsorbs molecularly and survives a second flush with pure CCl_4 (fourth from bottom, red trace): the peaks at 1128 and 1384 cm^{-1} associated with the adsorbed 6MeOQ are no longer visible in the IR spectra, and a new feature develop at 1462 cm^{-1} due to the quinuclidine C_7 CH_2 scissoring mode of Cd.[40] This ability of Cd to displace 6MeOQ from Pt surfaces was seen before with polycrystalline Pt foils.[41] Interestingly, though, re-exposure of the Cd-covered sample to a new solution of 6MeOQ (fifth from bottom, green) results in the coadsorption of some 6MeOQ with the Cd already present on the surface, as best indicated by the easy detection of strong peaks at 1388 (6MeOQ) and 1462 (Cd) cm^{-1} after flushing with CCl_4 (sixth from bottom, blue). In contrast, no 6MeOQ uptake at all was seen on the flat polycrystalline foil under similar circumstances.[41] The difference could be due to the limited volume available inside the titania shell of the yolk−shell nanocatalyst, but it is more likely explained by the different nature of the platinum surface in the polycrystalline foil versus the 5-nm-in-diameter nanoparticles. Regardless, it is clear that surface reactions involving more than one molecule can be easily driven on the surface of platinum nanoparticles embedded in yolk−shell nanostructures still.

3.3.3. H4C. Additional adsorption tests were carried out with a few other molecules of increasing sizes, listed in Table 1 and

shown schematically in Figure 4. Different tests contrasting the results from experiments with the core−shell and yolk−shell nanostructures versus those from different types of reference samples were tried to best assess adsorption on the metal surfaces. For instance, in Figure 7, the spectra from adsorption
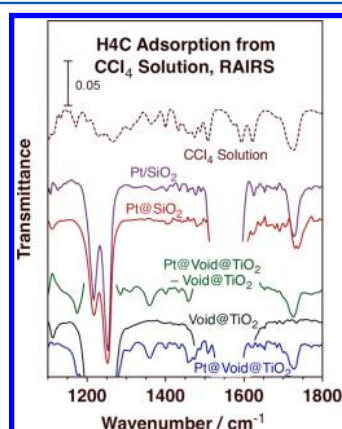

Figure 7. Transmission IR absorption spectra for H4C adsorbed on a conventional 1 wt % Pt/SiO₂ catalyst (second from top, solid purple trace), on Pt@SiO₂ (third from top, solid red), on Pt@Void@TiO₂ (bottom, solid blue), and on Void@TiO₂ (second from bottom, solid dark green). A difference spectrum between the last two is also provided to highlight the fact that the peaks seen in the bottom trace all correspond to adsorption on the platinum surface (third from bottom, solid light green). All these spectra were obtained by exposing the sample to a H4C/CCl₄ solution for 210 min and then flushing 5 times with pure CCl₄. A reference trace from a H4C/CCl₄ solution is provided as well (top, dashed magenta). Adsorption of H4C on the platinum surfaces of the Pt/SiO₂ and Pt@Void@TiO₂ samples is clear, with different geometries in each case, whereas the uptake on Pt@SiO₂ is limited at best.

of H4C on the Pt surfaces of Pt@SiO₂ (third from top, solid red trace) and Pt@Void@TiO₂ (bottom, solid blue) are contrasted with those obtained with a conventional 1 wt % Pt/SiO₂ catalysts (second from top, solid purple) and a Void@TiO₂ nanostructure (similar to the Pt@Void@TiO₂ sample but without the platinum nanocore; second from bottom, solid dark green). All the displayed spectra were acquired after flushing with CCl₄ to remove any dissolved or weakly adsorbed H4C; only the strongly adsorbed species are probed in this case. The IR traces from all three Pt-containing catalysts (but not from the Void@TiO₂ sample) display a sharp peak at 1400 cm⁻¹ (weaker, broader, and blue-shifted in the Pt@SiO₂ case) a feature also seen in the reference spectra from H4C in solution (top trace, dashed magenta line) that indicates that H4C adsorption does occur and that it is molecular in all cases. This band is absent in the spectrum of dihydroquinine[40] and may be related to an umbrella mode in the methyl moiety of the methoxy group bonded to the quinoline ring. Additional peaks are also detected at 1438, 1458, and ∼1480 cm⁻¹ with the Pt/SiO₂ and Pt@Void@TiO₂ samples. Those values are slightly shifted from the ones seen for H4C in solution, possibly because of the effect of the substrate, and are likely to all correspond to in-plane deformation modes within the hydro-quinine moiety, suggesting that adsorption may involve that side of the molecule. Finally, a large and broad signal is seen at around 1360 cm⁻¹ (possibly corresponding to a symmetric CH₃ umbrella mode) with the yolk−shell nanostructure but not with the conventional Pt/SiO₂ catalyst. Together, these

observations suggest that H4C can easily adsorb on the surfaces of Pt/SiO₂ and Pt@Void@TiO₂, although with different adsorption geometries: the detection of the three hydroquinine IR peaks suggests a tilted adsorption geometry in both cases, but the appearance of the 1360 cm⁻¹ only in the Pt@Void@ TiO₂ sample indicates different orientations for the quinucli-dine ring. Adsorption on Pt@SiO₂, on the other hand, is limited at best.

3.3.4. H4M2QE. The data for H4M2QE adsorption on the Pt@Void@TiO₂ and Void@TiO₂ samples are provided in Figure 8. Shown are IR traces for both nanostructures while
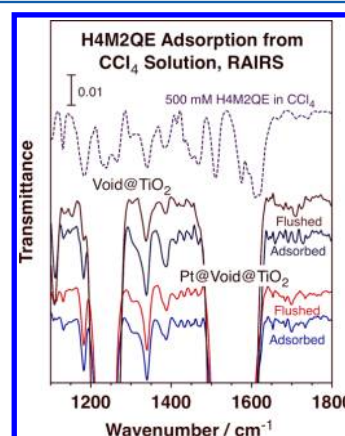

Figure 8. Transmission IR absorption spectra for H4M2QE adsorbed on Pt@Void@TiO₂ (bottom two traces) and Void@TiO₂ (next two traces from bottom) samples. Data are provided for the samples after immersing them in the H4M2QE/CCl₄ solution for 210 min (bottom and third from bottom solid, light and dark blue, traces, respectively) and after flushing 5 times with pure CCl₄ (second and fourth from bottom solid, light and dark red, traces, respectively). A reference trace from a H4M2QE/CCl₄ solution is provided as well (top, dashed magenta). Adsorption of H4M2QE dominates in this case, but some uptake on the platinum is also apparent.

immersed in a H4M2QE solution (bottom and third from bottom solid, light and dark blue, traces, respectively) and after flushing with CCl₄ (second and fourth solid, light and dark red, traces, respectively). In all cases, strong signals are seen at 1134, 1184, 1340, and 1388 cm⁻¹, all also present in the spectrum obtained for H4M2QE in solution (top dashed magenta trace). Those features are most likely associated with the 4-methoxy-2-quinolyl moiety, since they do not appear in the IR spectrum of H4C. The similarities of all the traces for the solid samples in comparison with that for the free dissolved molecules suggest minimal molecular distortion, but the fact that the signals do not go away upon flushing with the pure solvent still points to them originating from molecularly adsorbed species. Also, the spectra from the nanostructures with versus without the Pt nanocores look quite similar, indicating that the uptake mostly takes place on the titania shell. On the other hand, a degree of signal reduction in the 1184 and 1388 cm⁻¹ peaks, a reflection of some loss of adsorbed H4M2QE, is seen upon CCl₄ flushing with the Void@TiO₂ sample but not with the Pt@Void@TiO₂ one, indicating that there may be some adsorption on the Pt surface as well. The differences in relative IR peak intensities (only two out of four peaks show significant changes between the two samples) points to a defined adsorption geometry, but the minimal frequency shifts seen with respect to the free molecule indicate that the adsorption does not involve the auxiliary quinolyl moiety. Instead, the bonding may be through

the main quinoline ring in the hydroquinidine section of the molecule. Unfortunately, the main ring deformation vibrational modes for that moiety are masked by solvent peaks, so no definitive conclusion can be derived about the adsorption mode in this case.

3.3.5. (DHQ)2PHAL. In Figure 9, IR absorption spectra are shown for the adsorption of (DHQ)2PHAL on both silica and
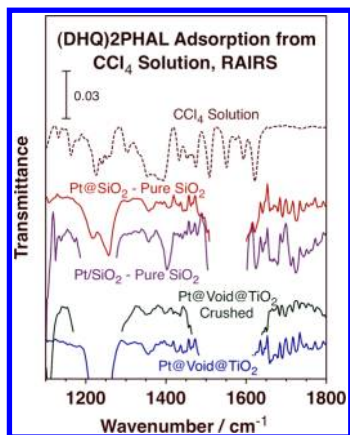

Figure 9. Transmission IR absorption spectra for (DHQ)2PHAL adsorbed on Pt@Void@TiO$_2$ samples, as prepared (bottom trace, solid blue) and after crushing the titania shells (second from bottom, solid green), and on a conventional 1 wt % Pt/SiO$_2$ sample (third from bottom, solid purple) and a Pt@SiO$_2$ catalyst (second from top, solid red) after subtracting the contribution from adsorption on pure SiO$_2$. All data were acquired after exposure to a (DHQ)2PHAL/CCl$_4$ solution for 210 min followed by 5 flushes with pure CCl$_4$. A reference trace from the (DHQ)2PHAL/CCl$_4$ solution is provided on top (dashed magenta trace). Adsorption of (DHQ)2PHAL/CCl$_4$ on the platinum surfaces seems to be unhindered by the titania and silica shells with this molecule as well.

titania based samples. In all four examples shown there, molecular adsorption on the platinum surface is best identified by the peak at about 1360 cm^{-1} and the accompanying shoulder at approximately 1370 cm^{-1}. Similar spectra were obtained with the Pt@Void@TiO$_2$ sample as prepared (bottom solid blue trace) versus after crushing the shells (second from bottom, solid green), done to facilitate access to the metal nanocores, which means that diffusion through the titania layers is not limiting for adsorption in this case. The examples with a silica support are reported here in differential mode, for a conventional 1 wt % Pt/SiO$_2$ (third from bottom, solid purple) and for Pt@SiO$_2$ (second from top, solid red) after subtraction of the contribution from pure SiO$_2$. It should be indicated that a small amount of weakly adsorbed (DHQ)2PHAL was seen on all supports upon exposure to (DHQ)2PHAL solutions, but that such species were easily removed upon flushing with pure CCl$_4$; all the data in this figure were acquired after multiple flushings with the pure solvent. Finally, a unique intense peak is also seen at 1400 cm^{-1} in the case of the Pt/SiO$_2$ sample, not evident with any of the other samples but similar to what is seen with H4C and H4M2QE (where it was assigned to an umbrella mode within the methoxy moiety, Figures 7 and 8, respectively). This suggests a unique adsorption geometry for the conventional catalysts, with the quinoline ring standing up on the surface and arranged so the methyl moiety in the methoxy group is oriented close to perpendicular to the metal surface.

3.3.6. ZnTPP. Our final test of mass transport through the oxide shells in the nanostructured samples was carried out by using ZnTPP, a typical porphyrin with an estimated diameter of almost 2 nm. Figure 10 displays the corresponding IR
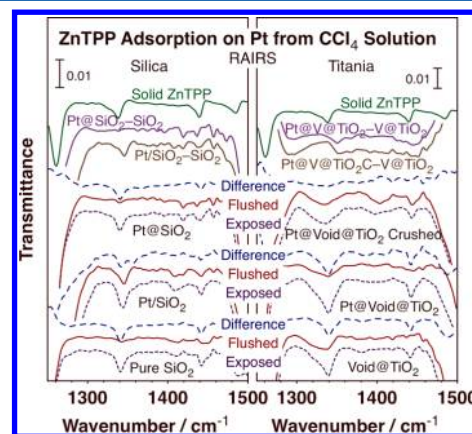

Figure 10. Transmission IR absorption spectra for ZnTPP adsorbed from CCl$_4$ solutions onto silica-based (left panel) and titania-based (right) samples. Sets of three traces are provided for each solid sample, obtained after 210 min exposures to the ZnTPP/CCl$_4$ solution (bottom, short-dashed purple lines) and following 5 flushes with pure CCl$_4$ (middle, solid red traces), and by subtraction of the two (top, long-dashed blue). The samples reported here are, from bottom to top, in the left panel: a pure silica powder, a conventional 1 wt % Pt/SiO$_2$ catalyst, and our Pt@SiO$_2$ core−shell sample; in the right panel: hollow titania shells and the Pt@Void@TiO$_2$ yolk−shell sample as prepared and after crushing of the shells (to increase access to the Pt nanocores). Relevant difference spectra are reported on top to highlight the adsorption on the platinum surfaces (second and third from top, brown and purple solid lines), and a reference trace is also provided for solid ZnTPP (top, solid green lines). Adsorption may be limited and geometrically constrained on the Pt surfaces of the core−shell and yolk−shell sample, but it is still possible.

absorption spectra for the silica-based (left panel) and titania-based (right) samples. The reference spectrum for solid ZnTPP shown at the top of both panels (solid green lines) is dominated by two skewed peaks at 1340 and 1440 cm^{-1}, associated with a metal-sensitive porphyrin ring in-plane deformation mode[42,43] and an out-of-plane mode of the terminal phenyl moieties,[44,45] respectively. Those peaks are also seen in the spectra obtained with all of our samples during their exposure to the ZnTPP/CCl$_4$ solution (short-dashed lines). However, in most instances, the majority of the IR intensities of those features go away upon flushing with pure CCl$_4$ (solid red traces); much of what is detected in these spectra can be assigned to ZnTPP either dissolved in the solvent or weakly adsorbed on the support.

Still, weaker but significant peaks persist upon flushing. This is particularly evident for the case of the conventional 1 wt % Pt/SiO$_2$ sample (Figure 10, left panel, second 3-trace data set from bottom), where a large peak at 1345 cm^{-1} is clearly retained throughout the flushing stage. An additional small peak is seen around 1340 cm^{-1} for the Pt@SiO$_2$ sample (left, third data set from bottom), and, perhaps more interestingly, new features also develop in the spectra with both platinum containing silica samples at 1427, 1436, and 1457 cm^{-1}. These peaks are weak but easy to see in the Pt@SiO$_2$−SiO$_2$ and Pt/SiO$_2$−SiO$_2$ difference spectra (left, second and third from the top, purple and brown solid lines, respectively). It would appear

H

dx.doi.org/10.1021/jp406991y | *J. Phys. Chem. C* XXXX, XXX, XXX−XXX

that ZnTPP can adsorb on the platinum surfaces of both silica-based samples, likely in molecular form but perhaps with some torsion of the terminal rings. A flatter adsorption geometry may be prevalent on the Pt@SiO$_2$ sample, since the strong 1340 cm^{-1} in-plane porphyrin deformation is not visible in the spectrum from that sample.

The data from the titania-based samples also seem to indicate some level of ZnTPP adsorption. The analysis here is complicated by the fact that ZnTPP appears to adsorb strongly on the titania surfaces as well, as indicated by the intense and broad peak seen around 1340 cm^{-1} in all cases, including with the empty titania shells (Figure 10, right panel). That peak is not removed by CCl$_4$ flushing. Adsorption on the titania surface does affect the infrared absorption spectra of the ZnTPP, a fact indicated by the observation that the main 1340 cm^{-1} feature red-shifts and becomes broader compared to the way it shows in the data for the solid, and also made evident by the fact that the other main vibrational band observed for the solid at 1440 cm^{-1} is absent in the data for the titania-adsorbed species.

Adsorption on platinum, which yields much weaker IR signals, is difficult to visualize in the raw spectra of the titania-based samples but becomes more clearly identified in the Pt@Void@TiO$_2$−Void@TiO$_2$ (Figure 10, right panel, third from top, solid brown line) and Pt@Void@TiO$_2$-crushed−Void@TiO$_2$ (right panel, second from top, solid purple line) traces. The most obvious piece of evidence for ZnTPP adsorption on Pt in these cases is the peak seen in the difference spectra at 1350 cm^{-1}. It is interesting to note that this is the same metal-sensitive band seen at 1340 cm^{-1} in the pure solid and at 1345 cm^{-1} with the silica-based samples. The reported understanding of these shifts is that the bands are displaced to the blue with increasing d-electron density,[46] which in this case suggests that adsorption of ZnTPP on the platinum surface involves electron donation from the Pt atoms of the surface to the Zn metal center of the porphyrin. The extent of this donation appears to be more extensive on the titania samples. Additional evidence for adsorption of the ZnTPP on the Pt nanocores of the Pt@Void@TiO$_2$ samples is provided by the small peaks seen in the 1400−1500 cm^{-1} range, although those are too small to make this statement conclusive.

3.3.7. Kinetic Data. The kinetics of the adsorption and desorption of all the molecules reported here support, in general, the main conclusion of this paper, that they all can access the surface of the platinum nanocores in the core−shell and yolk−shell nanostructures. A summary of these data is provided in Figure 11: the top row shows adsorption data as a function of exposure time to the given solutions, whereas the bottom row corresponds to experiments where the catalysts was flushed repeatedly with fresh solvent, for approximately an hour per cycle to allow for equilibration between the adsorbates and the thin liquid film right above the surface. For the adsorption of 6MeOQ, for instance, the left-top panel shows that saturation of both the Pt (1128 cm^{-1} peak, blue solid squares) and titania (1228 cm^{-1}, red open circles) surfaces in Pt@Void@TiO$_2$ occurs within 1−2 h of exposure to the 6MeOQ/CCl$_4$ solution, in a time frame comparable to that seen with CO (Figure 2). Also as in the case of the carbon monoxide uptake, saturation of the platinum surface precedes the saturation of the titania, pointing to the fact that the kinetics is controlled by mass transport of the whole liquid, solute plus solvent, through the shells, not by diffusion of the solute alone. The complementary data in the left-bottom panel of Figure 11
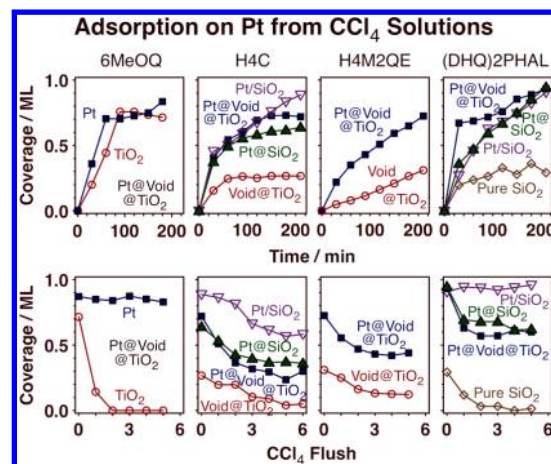

Figure 11. Kinetics of the uptake (top raw) and adsorbate removal versus number of CCl$_4$ flushings (bottom) of, from left to right, 6MeOQ (1128 and 1228 cm^{-1} peaks, for adsorption on Pt and titania, respectively), H4C (1622 cm^{-1}), H4M2QE (1180 cm^{-1}), and (DHQ)2PHAL (1622 cm^{-1}). Data are shown for our Pt@SiO$_2$ core−shell (green up-pointing triangles) and Pt@Void@TiO$_2$ yolk−shell (blue solid squares) samples as well as for a number of references: a conventional 1 wt % Pt/SiO$_2$ catalyst (purple down-pointing triangles), Void@TiO$_2$ hollow titania shells (red open circles), and a pure silica powder (brown open diamonds). In all cases, evidence is provided for the irreversible adsorption of the molecules on the Pt metal surface in addition of any reversible uptake that may occur on the support.

clearly illustrate the ease with which the 6MeOQ can be removed from the titania surface. The molecules adsorbed on the Pt substrate, on the other hand, are bonded more strongly and irreversibly and cannot be flushed out with the pure solvent.

The second column of Figure 11 corresponds to the uptake (top) and flushing (bottom) of H4C (1622 cm^{-1} peak) on Pt/SiO$_2$ (purple down-pointing open triangles), Pt@SiO$_2$ (green up-pointing solid triangles), Pt@Void@TiO$_2$ (blue solid squares), and Void@TiO$_2$ (red open circles) samples. The uptake on the Pt-containing samples all lead to final coverages at least twice those seen with the hollow titania shells, with that difference remaining on the samples after flushing the H4C adsorbed on the support (which does take several pure CCl$_4$ flushings). Similar trends are seen with Pt@Void@TiO$_2$ versus Void@TiO$_2$ with H4M2QE (1180 cm^{-1} peak, third column) and when contrasting the uptake of (DHQ)2PHAL (1622 cm^{-1} peak, fourth column) on Pt/SiO$_2$, Pt@SiO$_2$, or Pt@Void@TiO$_2$ versus on a pure silica powder (open brown diamonds). In all cases, additional adsorption on the platinum surfaces is observed, beyond any uptake possible on the support, and the difference in adsorption strength is indicated by the irreversible nature of the adsorption originating from the former, with signals that remain after multiple flushings with the pure solvent. Comparable uptake kinetic behavior, and in the same time frame, was observed with ZnTPP (data not shown).

4. CONCLUSIONS

Extensive in-situ infrared absorption spectroscopic characterization of the mass transport of molecules through the shells of core−shell (Pt@SiO$_2$) and yolk−shell (Pt@Void@TiO$_2$) nanostructures in liquid phase has indicated that such transport occurs readily with molecules of sizes of up to about 2 nm in

J

dx.doi.org/10.1021/jp406991y | *J. Phys. Chem. C* XXXX, XXX, XXX−XXX

diameter. The shells of these nanostructures display a dual pore distribution, with a majority of micropores of less than 1 nm in diameter and a secondary mesoporous structure with pore windows of approximately 4 nm in diameter. Our results strongly suggest that it may be the latter mesoporous network that provides a route for large molecules dissolved in liquid solvents to access the surface of the metal nanoparticles in the core of the core–shell and yolk–shell nanoarchitectures; it may not be possible to count on their microporosity to control mass transport in these structures. We believe that this, our main conclusion, is general and applies to most core–shell and yolk–shell nanostructures reported in the literature.

Adsorption on the metal was established by a combination of observations, including shifts in specific vibrational peaks (which also point to structural or electronic changes upon adsorption) and changes in relative peak intensities (reflecting specific adsorption geometries, even molecular distortions upon bonding to the surface). Adsorption on the metal was shown to be irreversible: the adsorbates could not be removed by flushing with pure solvent. This provided another way to discriminate against adsorption on the supports, which in most cases was proven to be reversible.

The kinetics of the transport of the molecules in solution through the porous oxide shells and of the uptake on the surface of the metallic nanocores could be estimated by following the peak intensities of key infrared absorption peaks, even if the time resolution was limited to approximately half an hour by an experimental factor, due to the limited flow of the solution through the thin space ($\sim$100 μm thickness) provided for the liquid to coexist with the solid. It was determined that the dominant effect for these adsorptions is not diffusion of the solute within the solution but rather mass transfer of the whole solute plus solvent through the shells. This leads to the counterintuitive result that saturation of the surface of the metal nanocores is often reached before saturation of the outer oxide shells. It was also established that the volume of the void spaces in the yolk–shell nanostructures is sufficiently large to allow for the displacement of one adsorbate by a second in a similar fashion as it occurs in an open system, without interferences because of the confined space provided for the solutions.

AUTHOR INFORMATION

Corresponding Author
*E-mail: zaera@ucr.edu (F.Z.).

Present Addresses
†J.L.: Key Laboratory for Advanced Materials and Research Institute of Industrial Catalysis, East China University of Science and Technology, Shanghai 200237, P. R. China.
‡X.L.: Key Laboratory of Mineralogy and Metallogeny, Guangzhou Institute of Geochemistry, Chinese Academy of Sciences.

Notes
The authors declare no competing financial interest.

REFERENCES

(1) Zaera, F. Nanostructured Materials for Applications in Heterogeneous Catalysis. *Chem. Soc. Rev.* **2013**, *42*, 2746–2762.
(2) Liu, S.; Han, M.-Y. Silica-Coated Metal Nanoparticles. *Chem.—Asian J.* **2010**, *5*, 36–45.
(3) Burns, A.; Ow, H.; Wiesner, U. Fluorescent Core-Shell Silica Nanoparticles: Towards "Lab on a Particle" Architectures for Nanobiotechnology. *Chem. Soc. Rev.* **2006**, *35*, 1028–1042.
(4) Lee, J.-H. Gas Sensors Using Hierarchical and Hollow Oxide Nanostructures: Overview. *Sens. Actuators, B* **2009**, *140*, 319–336.
(5) Zhang, Q.; Lee, I.; Joo, J. B.; Zaera, F.; Yin, Y. Core–Shell Nanostructured Catalysts. *Acc. Chem. Res.* **2012**, *46*, 1816–1824.
(6) Hirsch, L. R.; Jackson, J. B.; Lee, A.; Halas, N. J.; West, J. L. A Whole Blood Immunoassay Using Gold Nanoshells. *Anal. Chem.* **2003**, *75*, 2377–2381.
(7) Zhu, Y.; Shi, J.; Shen, W.; Dong, X.; Feng, J.; Ruan, M.; Li, Y. Stimuli-Responsive Controlled Drug Release from a Hollow Mesoporous Silica Sphere/Polyelectrolyte Multilayer Core–Shell Structure. *Angew. Chem., Int. Ed.* **2005**, *44*, 5083–5087.
(8) Gao, J.; Liang, G.; Zhang, B.; Kuang, Y.; Zhang, X.; Xu, B. Fept@ CoS$_2$ Yolk–Shell Nanocrystals as a Potent Agent to Kill Hela Cells. *J. Am. Chem. Soc.* **2007**, *129*, 1428–1433.
(9) Luo, J.; Wang, L.; Mott, D.; Njoki, P. N.; Lin, Y.; He, T.; Xu, Z.; Wanjana, B. N.; Lim, I. I. S.; Zhong, C.-J. Core/Shell Nanoparticles as Electrocatalysts for Fuel Cell Reactions. *Adv. Mater.* **2008**, *20*, 4342–4347.
(10) De Rogatis, L.; Cargnello, M.; Gombac, V.; Lorenzut, B.; Montini, T.; Fornasiero, P. Embedded Phases: A Way to Active and Stable Catalysts. *ChemSusChem* **2010**, *3*, 24–42.
(11) Jia, C.-J.; Schüth, F. Colloidal Metal Nanoparticles as a Component of Designed Catalyst. *Phys. Chem. Chem. Phys.* **2011**, *13*, 2457–2487.
(12) Su, L.; Jing, Y.; Zhou, Z. Li Ion Battery Materials with Core-Shell Nanostructures. *Nanoscale* **2011**, *3*, 3967–3983.
(13) Oldfield, G.; Ung, T.; Mulvaney, P. Au@SnO$_2$ Core–Shell Nanocapacitors. *Adv. Mater.* **2000**, *12*, 1519–1522.
(14) Caruso, F. Nanoengineering of Particle Surfaces. *Adv. Mater.* **2001**, *13*, 11–22.
(15) Reiss, P.; Protière, M.; Li, L. Core/Shell Semiconductor Nanocrystals. *Small* **2009**, *5*, 154–168.
(16) Schärtl, W. Current Directions in Core-Shell Nanoparticle Design. *Nanoscale* **2010**, *2*, 829–843.
(17) Yin, Y.; Rioux, R. M.; Erdonmez, C. K.; Hughes, S.; Somorjai, G. A.; Alivisatos, A. P. Formation of Hollow Nanocrystals through the Nanoscale Kirkendall Effect. *Science* **2004**, *304*, 711–714.
(18) Lou, X. W.; Archer, L. A.; Yang, Z. Hollow Micro-/Nanostructures: Synthesis and Applications. *Adv. Mater.* **2008**, *20*, 3987–4019.
(19) Zhang, Q.; Lee, I.; Ge, J.; Zaera, F.; Yin, Y. Surface-Protected Etching of Mesoporous Oxide Shells for Stabilization of Metal Nanocatalysts. *Adv. Funct. Mater.* **2010**, *20*, 2201–2214.
(20) Kim, S.; Yin, Y.; Alivisatos, A. P.; Somorjai, G. A.; Yates, J. T. Ir Spectroscopic Observation of Molecular Transport through Pt@CoO Yolk–Shell Nanostructures. *J. Am. Chem. Soc.* **2007**, *129*, 9510–9513.
(21) Lee, I.; Joo, J. B.; Yin, Y.; Zaera, F. A Yolk@Shell Nanoarchitecture for Au/TiO$_2$ Catalysts. *Angew. Chem., Int. Ed.* **2011**, *50*, 10208–10211.
(22) Andanson, J.-M.; Baiker, A. Exploring Catalytic Solid/Liquid Interfaces by in Situ Attenuated Total Reflection Infrared Spectroscopy. *Chem. Soc. Rev.* **2010**, *39*, 4571–4584.
(23) Zaera, F. Surface Chemistry at the Liquid/Solid Interface. *Surf. Sci.* **2011**, *605*, 1141–1145.
(24) Zaera, F. Probing Liquid/Solid Interfaces at the Molecular Level. *Chem. Rev.* **2012**, *112*, 2920–2986.
(25) Liang, X.; Li, J.; Joo, J. B.; Gutiérrez, A.; Tillekaratne, A.; Lee, I.; Yin, Y.; Zaera, F. Diffusion through the Shells of Yolk–Shell and Core–Shell Nanostructures in the Liquid Phase. *Angew. Chem., Int. Ed.* **2012**, *51*, 8034–8036.

(26) Lee, I.; Albiter, M. A.; Zhang, Q.; Ge, J.; Yin, Y.; Zaera, F. New Nanostructured Heterogeneous Catalysts with Increased Selectivity and Stability. *Phys. Chem. Chem. Phys.* **2011**, *13*, 2449−2456.

(27) Joo, J. B.; Zhang, Q.; Dahl, M.; Zaera, F.; Yin, Y. Synthesis, Crystallinity Control, and Photocatalysis of Nanostructured Titanium Dioxide Shells. *J. Mater. Res.* **2013**, *28*, 362−368.

(28) Kubota, J.; Ma, Z.; Zaera, F. In-Situ Characterization of Adsorbates in Solid-Liquid Interfaces by Reflection-Absorption Infrared Spectroscopy. *Langmuir* **2003**, *19*, 3371−3376.

(29) Greenler, R. G. Infrared Study of Adsorbed Molecules on Metal Surfaces by Reflection Techniques. *J. Chem. Phys.* **1966**, *44*, 310−315.

(30) Hoffmann, F. M. Infrared Reflection-Absorption Spectroscopy of Adsorbed Molecules. *Surf. Sci. Rep.* **1983**, *3*, 107−192.

(31) Albiter, M. A.; Crooks, R. M.; Zaera, F. Adsorption of Carbon Monoxide on Dendrimer-Encapsulated Platinum Nanoparticles: Liquid Versus Gas Phase. *J. Phys. Chem. Lett.* **2010**, *1*, 38−40.

(32) Dillon, R. J.; Joo, J.-B.; Zaera, F.; Yin, Y.; Bardeen, C. J. Correlating the Excited State Relaxation Dynamics as Measured by Photoluminescence and Transient Absorption with the Photocatalytic Activity of Au@TiO$_2$ Core-Shell Nanostructures. *Phys. Chem. Chem. Phys.* **2013**, *15*, 1488−1496.

(33) Albiter, M. A.; Zaera, F. Adsorption Properties of Supported Platinum Catalysts Prepared Using Dendrimers. *Langmuir* **2010**, *26*, 16204−16210.

(34) Lee, I.; Ge, J.; Zhang, Q.; Yin, Y.; Zaera, F. Encapsulation of Supported Pt Nanoparticles for Increased Catalyst Stability. *Nano Res.* **2011**, *4*, 115−123.

(35) Zaera, F. Infrared Absorption Spectroscopy of Adsorbed CO: New Applications in Nanocatalysis for an Old Approach. *ChemCatChem* **2012**, *4*, 1525−1533.

(36) Mallat, T.; Orglmeister, E.; Baiker, A. Asymmetric Catalysis at Chiral Metal Surfaces. *Chem. Rev.* **2007**, *107*, 4863−4890.

(37) Zaera, F. Chiral Modification of Solid Surfaces: A Molecular View. *J. Phys. Chem. C* **2008**, *112*, 16196−16203.

(38) Gordon, A. D.; Zaera, F. Adsorption of 1-(1-Naphthyl)-Ethylamine from Solution onto Platinum Surfaces: Implications for the Chiral Modification of Heterogeneous Catalysts. *Angew. Chem., Int. Ed.* **2013**, *52*, 3453−3456.

(39) Ma, Z.; Lee, I.; Zaera, F. Factors Controlling Adsorption Equilibria from Solution onto Solid Surfaces: The Uptake of Cinchona Alkaloids on Platinum Surfaces. *J. Am. Chem. Soc.* **2007**, *129*, 16083−16090.

(40) Chu, W.; LeBlanc, R. J.; Williams, C. T.; Kubota, J.; Zaera, F. Vibrational Band Assignments for the Chiral Modifier Cinchonidine: Implications for Surface Studies. *J. Phys. Chem. B* **2003**, *107*, 14365−14373.

(41) Ma, Z.; Zaera, F. Competitive Chemisorption between Pairs of Cinchona Alkaloids and Related Compounds from Solution onto Platinum Surfaces. *J. Am. Chem. Soc.* **2006**, *128*, 16414−16415.

(42) Andersson, L. A.; Loehr, T. M.; Thompson, R. G.; Strauss, S. H. Influence of Symmetry on the Vibrational Spectra of Zn(TPP), Zn(TPC), and Zn(TPIBC). *Inorg. Chem.* **1990**, *29*, 2142−2147.

(43) Zhang, Y.-H.; Zhao, W.; Jiang, P.; Zhang, L.-J.; Zhang, T.; Wang, J. Structural Parameters and Vibrational Spectra of a Series of Zinc Meso-Phenylporphyrins: A Dft and Experimental Study. *Spectrochim. Acta, Part A* **2010**, *75*, 880−890.

(44) Minaev, B.; Lindgren, M. Vibration and Fluorescence Spectra of Porphyrin-Cored 2,2-Bis(Methylol)-Propionic Acid Dendrimers. *Sensors* **2009**, *9*, 1937−1966.

(45) Kozlowski, P. M.; Rush, T. S.; Jarzecki, A. A.; Zgierski, M. Z.; Chase, B.; Piffat, C.; Ye, B.-H.; Li, X.-Y.; Pulay, P.; Spiro, T. G. DFT-SQM Force Field for Nickel Porphine: Intrinsic Ruffling. *J. Phys. Chem. A* **1999**, *103*, 1357−1366.

(46) Kincaid, J.; Nakamoto, K. Vibrational Spectra of Transition Metal Complexes of Tetraphenylporphine. *J. Inorg. Nucl. Chem.* **1975**, *37*, 85−89.

K

dx.doi.org/10.1021/jp406991y | *J. Phys. Chem. C* XXXX, XXX, XXX−XXX